Ultrafast and Nonlinear Spectroscopy of Solids with Small Energy Photons

J. Kono

Department of Electrical and Computer Engineering, Rice Quantum Institute, and
Center for Nanoscale Science and Technology, Rice University, Houston, Texas 77005, U.S.A.

Ultrashort pulses of intense, coherent, and tunable far-infrared (FIR) and mid-infrared (MIR) radiation, achievable with free-electron lasers (FELs) and optical parametric amplifiers (OPAs), provide unique opportunities to investigate low energy dynamics in solids. This paper reviews our recent experiments on bulk and quantum-confined semiconductors using such radiation. These experiments include: FIR spectroscopy of transient plasmas and magneto-plasmas, picosecond time-resolved cyclotron resonance, sideband and harmonic generation, the dynamical Franz-Keldysh effect, and AC ionization dynamics of quantum-well excitons.

KEYWORDS: infrared, free electron lasers, semiconductors, ultrafast and nonlinear optics

1. Introduction

The advent of long-wavelength coherent sources, such as free-electron lasers (FELs),[1] optical parametric amplifiers (OPAs),[2] and Terahertz (THz) antennas,[3] has created a new class of opportunities to study small-energy phenomena in solids in the time domain and/or high-intensity regimes. In particular, far-infrared (FIR) pulses can directly excite low-energy dynamics in bulk and quantum-confined semiconductors, e.g., cyclotron resonance (CR),[4-9] internal transitions of shallow donors[10-12] and excitons,[13-15] phonons,[16,17] and intersubband transitions.[18-22] In addition, small photon energies enhance the ponderomotive potential energy[15,23] while minimizing interband absorption and sample damage, leading to *extreme* nonlinear optical behavior in semiconductors.[23,24] Furthermore, intraband FIR/THz spectroscopy is independent of whether the states involved are interband-active or not, thus providing a rare opportunity to directly probe nonradiative (or "dark") states.

This paper will review our recent experiments on bulk and quantum-confined semiconductors using FIR and MIR radiation that clearly demonstrate these advantages. Most of the experiments were carried out by two-color methods, i.e., using a synchronized FIR – near-infrared (NIR) system or a MIR – NIR system, which allowed us to couple intra- and interband dynamics simultaneously.

2. Experimental methods

2-1. Synchronized FEL/Ti:Sapphire system

In the experiments described in Sections 3, 4 and 5, we utilized the unique characteristics of the Stanford FEL, i.e., the wide spectral range (3 - 80 µm), the short pulse duration (0.6 - 5 ps), and the high peak powers (up to 2 MW). The output consisted of "macropulses" with the repetition rate of 5 - 20 Hz, which, in turn, contained picosecond "micropulses" at 11.8 MHz. The NIR radiation was provided by a regenerative amplifier seeded by a mode-locked Ti:Sapphire laser, which was driven at the seventh harmonic (82.6 MHz) of the micropulse repetition rate (11.8 MHz). The temporal overlap between the two beams was adjustable using the synchronization electronics and a delay stage.

2-2. Time-resolved cyclotron resonance setup

The experimental setup for the picosecond time-resolved cyclotron resonance (TRCR) experiments is illustrated schematically in Fig. 1.
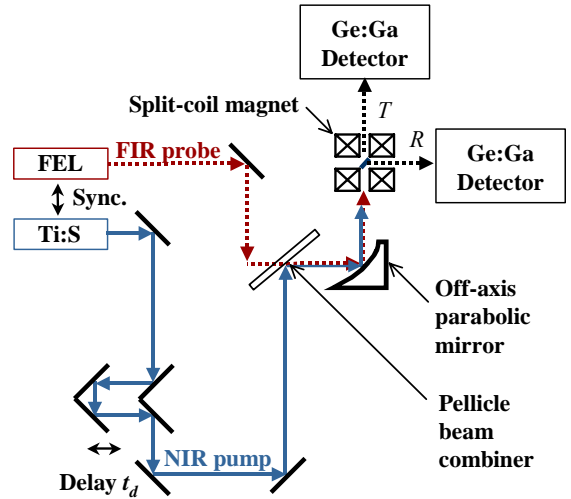

Fig. 1. Experimental setup for two-color, NIR-pump–FIR-probe spectroscopy of semiconductors in magnetic fields. The transmission and reflection of the FIR beam can be recorded as simultaneous functions of time delay and magnetic field.

The NIR pump beam from the Ti:Sapphire system was directed through a computer-controlled variable delay stage, after which it was spatially overlapped with the FIR beam from the FEL using a Pellicle plate. The two beams were thus made collinear as they were focused onto the sample using a parabolic mirror. The NIR pulse excited nonequilibrium carriers across the band gap of the sample, which then absorbed a fraction of the incident FIR probe pulse. The transmitted and reflected FIR beams were then recollimated and directed to liquid-helium-cooled Ge:Ga photoconductive detectors. Our synchronization electronics allowed us to obtain a single NIR pulse per FEL macropulse. With this arrangement, we were able to compare the intensities of the transmitted and reflected FIR pulses before and after the NIR pump pulse. The amounts of photo-induced change in FIR transmission and reflection were thus recorded as functions of time delay and magnetic field.

2-3. Sideband generation setup

We used a similar setup for THz sideband generation with the major difference being that the pump is now the FEL beam and the probe is the Ti:Sapphire beam. We focused the NIR-THz collinear beams onto the sample using an off-axis parabolic mirror down to ~ 0.5 mm. The sample was placed in a helium-flow optical cryostat equipped with a variable temperature control (T = 20 - 300 K). The transmitted and emitted radiation was transported and focused into a NIR spectrometer equipped with a Si CCD. The spectral resolution of the system was ~ 1.3 nm (or 2.6 meV). The spectrometer shutter was controlled by the macropulse trigger, but the shutter was usually left open for a time of many (16-80) macropulses, depending on the signal intensity and repetition rate. The THz power was monitored *in situ* and averaged during a single acquisition cycle. Most of the measurements were made with the sample rotated along the vertical axis to ~ 45° with respect to the propagation direction of the incident beams. The polarization of the THz (NIR) beam was usually kept horizontal but could be rotated using a polarizer pair (a half-wave plate).

2-4. Samples studied

The bulk InSb sample used in the first two experiments was undoped and had an electron density of 8.0×10^{13} cm^{-3} and a 77 K mobility of 8.3×10^{5} cm^{2}V^{-1}s^{-1}. The InSb quantum well (QW) sample used in the TRCR study was an undoped multiple QW (MQW) structure, containing 25 periods of 35 nm InSb wells separated by 50 nm thick Al$_{0.09}$In$_{0.91}$Sb barriers, grown by molecular beam epitaxy on a semi-insulating (001) GaAs substrate. The sample growth procedures and basic sample characteristics have been described previously.[25] Because of the lattice mismatch between the well and the barrier materials (~0.5%), the wells were under compressive strain. The bulk GaAs sample used in the first three experiments was purchased from American Xtal Technology; it was semi-insulating, with excess arsenic. The sample used for the exciton ionization study was an undoped InGaAs/GaAs MQW structure grown on a semi-insulating GaAs substrate. The MQW contained 15 periods, where each period consisted of an 8 nm In$_{0.2}$Ga$_{0.8}$As quantum well and 15 nm GaAs barrier. The growth temperature was 540°C and the InGaAs composition was calibrated by X-ray diffraction on a separate sample.

3. Far-infrared dynamics of transient plasmas

Here we studied the FIR properties of photo-generated transient plasmas in semiconductors using the above-described synchronized FIR-NIR laser system with picosecond time resolution, both in the absence and presence of an external magnetic field. We simultaneously monitored the time evolution of the transmission and reflection of a FIR probe pulse after NIR excitation. This allowed us to carry out a *dynamical* study of the Drude conductivity of photocreated transient plasmas. More specifically, we were

able to directly determine the density and scattering lifetime of the carriers as functions of time, i.e., $n(t)$ and $\tau(t)$.

Typical time-resolved FIR data for GaAs and InSb are shown in Fig. 2. The transmission, reflection, and absorption of the FIR probe beam are plotted against time delay. The wavelength of the FIR probe was 42 μm and the sample temperature was 1.5 K. Different traces correspond to different NIR intensities, with the maximum NIR fluence at the sample estimated to be ~ 4 mJ/cm^2. The NIR pump pulse is incident on the sample at time zero. The FIR probe pulse then arrives at the sample after a delay and is absorbed by the carriers created by the pump. In both the GaAs and InSb samples, the photogenerated carriers cause an abrupt drop (rise) in the FIR transmission (reflection) at timing zero. For example, at the maximum NIR intensity, the transmission drop is 100% (complete transmission quenching) in GaAs and ~ 70% in InSb. The photo-induced absorption curves shown were obtained from the measured transmission and reflection curves using the formula,

$$\Delta A = \frac{1-R-T}{1-R} - \frac{1-R_0-T_0}{1-R_0}, \quad (1)$$

where R and T are the reflectance and transmittance, respectively, and R_0 and T_0 are the values before the arrival of the NIR pump pulse.
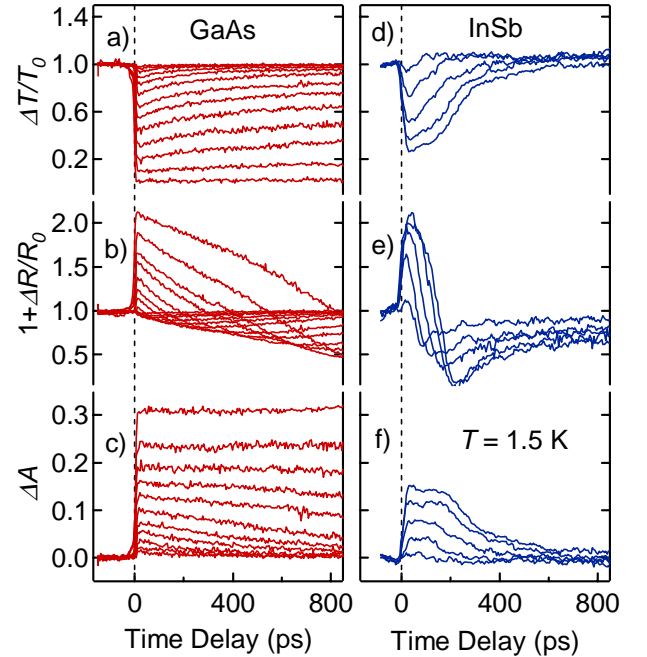

Fig. 2. Time evolution of photo-induced changes in FIR transmission, reflection, and absorption for different NIR pump intensities in GaAs (left: a-c) and InSb (right: d-f). The wavelength of the FIR probe was 42 μm, that of the NIR pump was 800 nm, and the sample temperature was 1.5 K.

The photo-induced reflectivity change is not a simple function of time delay or NIR pump intensity. Both its magnitude and sign depend on these parameters in a complicated manner. In addition, this behavior is material-dependent [cf. Fig. 2(b) vs. Fig. 2(e)]. Detailed analysis of reflectivity dy-

namics should provide a wealth of information on the dynamics of photogenerated carriers.

We developed a theory for the reflectivity of a transient plasma as a function of carrier density (n), scattering time (τ), and magnetic field (B). After being created by the NIR laser beam, the carrier population decreases on a picosecond time scale. While there are a number of possible decay mechanisms, the dominant one, especially in narrow gap semiconductors at high carrier densities, is known as Auger recombination, in which an electron and a hole recombine and the resulting energy is transferred to a third carrier. In this decay mechanism, the carrier density decreases in a characteristic way:

$$\frac{dn}{dt} = -C_2 n^2 , \quad (2)$$

where $C_2 = 7.5 \times 10^{-9}$ cm^{3}s^{-1} is the known Auger coefficient for InSb. In our analyses we used a modified Auger coefficient $C_2^* = \kappa C_2$ in order to account for other decay processes which are not explicitly taken into account in our model, such as carrier diffusion and radiative recombination. The density evolution $n(t)$ is then given by

$$n(t) = \frac{1}{C_2^* t + 1/n(0)} \quad (3)$$

where $n(0)$ denotes the initial density of the photocreated electron-hole pairs. The scattering rate τ^{-1} is taken to be a power law function of the density n, with coefficient α, exponent β and a small fixed offset $\tau_i \sim 0.1$ ps used to account for density-independent scattering mechanisms:

$$\frac{1}{\tau} = \alpha n^\beta + \frac{1}{\tau_i} . \quad (4)$$

The dielectric function of the nonequilibrium electron plasmas is given by:

$$\varepsilon_\omega(t) = \varepsilon_\infty \left[1 + \varepsilon_{ph}(\omega) - \frac{\omega_p(t)^2}{\omega\{\omega - i/\tau(t)\}} \right] . \quad (5)$$

Here $\varepsilon_\infty = 15.68$ is the dielectric constant for InSb, $\omega_p = \{4\pi n(t)e^2/m^*\}^{1/2}$ is the plasma frequency ($m^* = 0.014m_0$). The phonon contribution $\varepsilon_{ph}(\omega)$ is given by:

$$\varepsilon_{ph}(\omega) = \frac{\omega_L^2 - \omega_T^2}{\omega_T^2 - \omega^2 + i\Gamma\omega} , \quad (6)$$

where $\omega_L = 23.6$ meV ($\omega_T = 22.2$ meV) is the frequency of the longitudinal (transverse) optical phonon and $\Gamma = 0.35$ meV. At 45 degrees incidence, the reflection coefficient r_ω can be calculated using a Fresnel formula:

$$r_\omega(t) = \frac{\varepsilon_\omega \cos(\pi/4) - \sqrt{\varepsilon_\omega - \sin^2(\pi/4)}}{\varepsilon_\omega \cos(\pi/4) + \sqrt{\varepsilon_\omega - \sin^2(\pi/4)}} . \quad (7)$$

The normalized photoinduced reflectivity change due to transient plasmas is then computed as:

$$\frac{R(t)}{R_0} = 1 + \frac{\Delta R(t)}{R_0} = \frac{r_\omega(t) r_\omega^*(t)}{r_\omega(\infty) r_\omega^*(\infty)} , \quad (8)$$

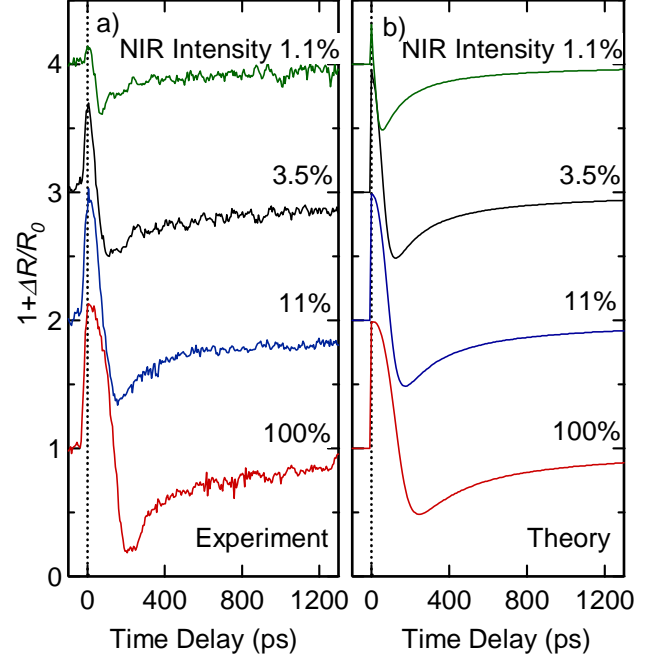where $R_0 = |r(\infty)|^2$ is the reflectivity in equilibrium (~0.198 for InSb and ~0.3 for GaAs).

Fig. 3. Experimental (a) and calculated (b) photo-induced reflectivity of InSb as a function of time delay for selected NIR pump intensities.
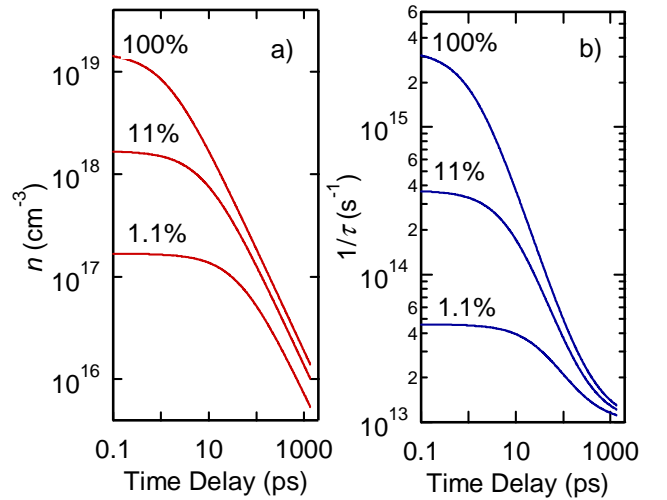

Fig. 4. Time evolution of the density (a) and scattering rate (b) in InSb deduced from the fitting analysis shown in Fig. 3 and described in detail in the text.

In Fig. 3, we present our experimental data (panel a) along with the fits (panel b) obtained using Eq. (8). We first point out that using the initial rise of the reflectivity, i.e., $\Delta R(0)/R_0$ we were able to determine the initial carrier density, as well as the parameters α and β in Eq. (4). The initial density of photocreated carriers $n(0)$ scales linearly with the pump intensity, as expected. We also found that most fits result in a value of β very close to 1, suggesting the importance of electron-electron scattering.[26] The resulting expres-

sion for the scattering rate is as follows: $1/\tau \sim 2.1 \times 10^{-4}$ n [cm^{-3}]. Using this expression for all NIR intensities, we then performed time-evolution fits assuming the Auger-like decay of the carrier population [cf. Eq. (3)]. The multiplicative factor κ showed a rather weak, but systematic, decrease from ~ 17 to ~ 7 with increasing NIR intensity. In Fig. 4 we present the time evolution of the carrier density (a) and the scattering rate (b) calculated using Eqs. (3) and (4) with the parameters derived from the fits.

When an external magnetic field is applied, Eq. (5) is modified, for CR active (+) and inactive (−) polarizations, respectively, into:

$$\varepsilon_{\omega,\pm}(t) = \varepsilon_\infty \left[1 + \varepsilon_{ph}(\omega) - \frac{\omega_p(t)^2}{\omega\{\omega \pm \omega_c - i/\tau(t)\}} \right], \quad (9)$$

where $\omega_c = eB/m$ is the cyclotron frequency. Equation (8) changes accordingly. Figure 5 illustrates (a) experimental and (b) theoretical magneto-plasma reflection dynamics, showing interesting interplay between ω_p and ω_c. The data at $B = 0$ T shows a reflectivity *drop* due to the created carriers. This behavior is due to the fact that the ω_p of the created carriers is lower than the FIR photon frequency. When this is the case, an increased carrier density translates into a decreased refractive index, and hence, a decreased reflectivity. However, this behavior very quickly disappears as we increase B from 0 to 1.5 T. A small peak appears in reflectivity, which grows in intensity with increasing B, reaching a maximum at ~ 3 T, stays roughly constant up to ~ 5 T, and finally goes away at higher B. This very interesting behavior is explainable in terms of the tuning of ω_p by B,[27] or the interplay between ω_p and ω_c, and is successfully reproduced by our model [Fig. 5(b)].
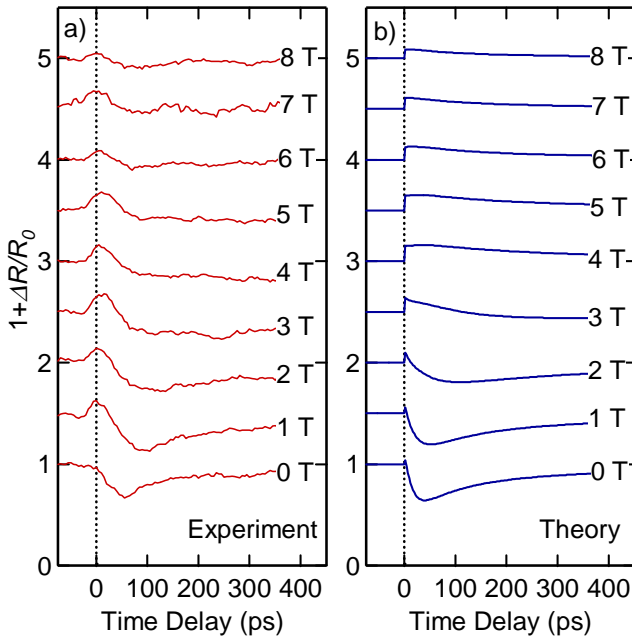

Fig. 5. Measured (a) and calculated (b) time-resolved photo-induced reflection in InSb at a range of fixed magnetic fields.

4. Time-resolved cyclotron resonance

Here we describe results of our time-resolved cyclotron resonance (TRCR) study of bulk InSb and InSb/AlInSb quantum wells (sample details are described in Section 2.4). InSb was chosen for the picosecond TRCR technique for the following reasons: 1) InSb has very small carrier effective masses which allow us to perform electron TRCR measurements in the magnetic field and FIR wavelength range available to us, and 2) the Landau level structure of InSb has been well-studied.[28] The TRCR experiment allows us to directly monitor the time evolution of the effective mass, carrier density, and scattering time of photo-created, non-equilibrium carriers in the presence of a magnetic field.
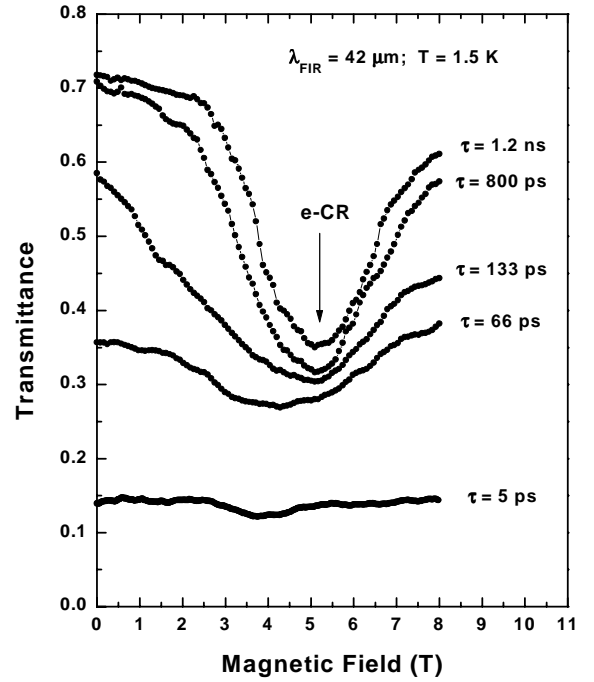

Fig. 6. Picosecond time-resolved CR of photo-created non-equilibrium electrons in InSb. The magnetic field is scanned at fixed time delays.

Figure 6 shows TRCR data obtained at a variety of fixed time delays. It displays two interesting features. First, there is no well-defined resonance at the smallest measured time scale. In this time regime (a few picoseconds after the creation of a high density of non-equilibrium free carriers), the carrier scattering rate is high enough to broaden the CR peak until it is completely obscured (i.e., the mean time between collisions τ is smaller than $1/\omega_c$). The observed TRCR linewidths are much larger than the transform limited spectral width of the picosecond FIR pulse, which, at 3.6 meV, corresponds to a CR line-width of only ~0.6 T in InSb. Second, the CR peak position moves toward higher magnetic fields as a function of time delay. This is indicative of an electron effective mass that *increases* as a function of time, which is opposite of the behavior expected due to the strong non-parabolicity of the InSb conduction band. The effective masses of carriers in the InSb conduction band increase with increasing energy. With 800 nm (laser) excitation, the initially excited carriers are well above the band edge. Therefore, one would expect that as the carriers relax toward the

band edge, their effective mass should decrease, thereby shifting the CR peak toward lower magnetic fields. The behavior displayed in the data is clearly opposed to these assertions, and requires further explanation.

Typical TRCR data for InSb/InAlSb multiple quantum wells are shown in Fig. 7(a) for six different fixed delays. We can see a smooth evolution of CR from 25 ps to 1.3 ns. At 25 ps after excitation, the CR line is significantly broadened to higher B, i.e., to a heavier effective mass. As time progresses, the electrons relax towards the band edge, resulting in a lighter mass at 1.3 ns. The average cyclotron mass and average scattering time, obtained through Lorentzian fits to the traces in (a), are plotted vs. delay in Figs. 7(b) and (c), respectively, presenting the CR dynamics stated above more quantitatively.
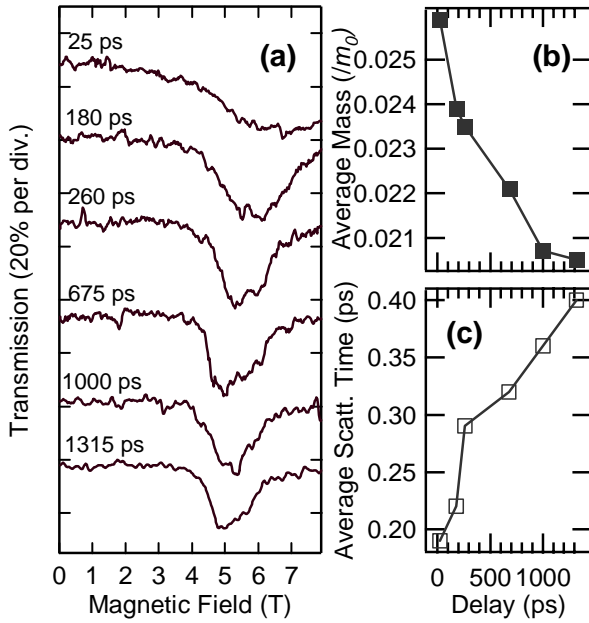

Fig. 7. Picosecond time-resolved CR of photo-created electrons in InSb quantum wells. The magnetic field is scanned at fixed time delays. (a) Transmission change of the FIR probe pulse as a function of magnetic field at different time delays. The wavelength of the probe was 42 μm, the sample temperature was 1.5 K, and the NIR fluence was ~ 1.3 mJ/cm². (b) Average cyclotron mass vs. time delay. (c) Average momentum scattering time vs. time delay.

We performed a detailed simulation of the TRCR spectra obtained for 42 μm probe light, as shown in Fig. 8. The fixed parameters in the simulation were the calculated B positions of the CR transitions and, at each time delay, the carrier density and scattering time, taken from fits to the data. The variable parameter was the temperature of the Fermi-Dirac distribution of excited carriers. We neglected continuum states above the barrier energy and many-body effects such as band gap renormalization. We also took into account the reduction in CR-active population that occurs when the upper level of a transition is populated. The results accurately reproduced the observed features, which arise from the strong conduction band nonparabolicity. Namely, the initially excited carriers, having a high carrier temperature, populate states with high Landau indices, where the cyclotron masses are higher than that of the lowest electron

Landau level. This is the main cause for the significant initial broadening (inhomogeneous broadening). As time progresses, the electrons relax toward the lowest Landau level (inter-Landau-level relaxation), and, as a result, the number of transitions contributing to the observed linewidth decreases in time. In addition, the linewidth of individual CR transitions decreases with time. This indicates that each energy level is initially broadened due to the high scattering rate in the high density and high temperature regime (homogeneous broadening). As time progresses, both the electron temperature and density decrease, making individual transitions narrower. The simulation was not representative at very short time delays (< 200 ps) because it did not include the dynamics of highly-excited carriers relaxing into the well.

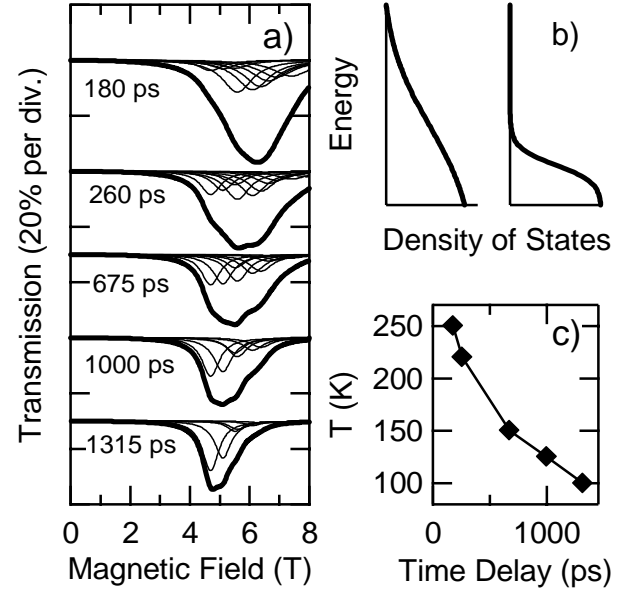**Fig. 8**. (a) Simulated TRCR spectra for the traces in Fig. 6, based on the energy levels shown in Fig. \ref{fan}. Simulation successfully reproduces the main observed features arising from nonparabolicity. (b) Cartoon at left (right) shows a Fermi distribution at short (long) time delay, when the carrier population is large and hot (small and cold). (c) Simulated carrier temperature as a function of time delay.

5. Terahertz sideband generation

The properties of semiconductors can be drastically modified when they are subjected to an intense external electric field. In particular, intense fields can significantly modify optical properties, leading to various electro-optical phenomena in semiconductors. Here we report on the generation of THz sidebands from a bulk GaAs crystal. In this multiphoton process, a weak optical or NIR beam passes through a THz-driven semiconductor, acquiring strong emission lines, or optical THz sidebands, with frequencies separated by integer multiples of the THz frequency:

$$\omega_n = \omega_{NIR} \pm n\omega_{THz}, \quad n = 1,2,3,... \quad (10)$$

It was previously demonstrated[14] that these lines completely dominate the near-bandedge emission properties of THz-

driven semiconductors. Recent theoretical studies predicted intriguing phenomena for THz sidebands such as dynamical symmetry breaking,[29] non-monotonic power dependence,[30] chaotic behavior, sideband disappearance under cyclotron resonance,[30] and THz-induced subband hybridization.[31] None of these have been observed to date, however.

Previous observation of THz sidebands in semiconductors relied on *resonant enhancement* using either magnetoexciton states[14] or quantum well subband states.[32] Since the intensity of THz field remained rather weak, the main results were successfully explained by perturbation theory.[33] In the work by Phillips *et al.*[32] the inversion symmetry of the system was intentionally broken, allowing the detection of odd ($n = \pm 1$) sidebands, whereas in the work by Kono *et al.*[14] only even ($n = \pm 2, \pm 4$) sidebands were observed. In either case, presumably due to the resonant nature and smaller intensities used, there was no signature of *bulk* $\chi^{(2)}$ contribution, which should always exist even in quantum well samples. Finally, both previous studies were essentially CW, and thus did not provide any information on the evolution of sidebands in the time domain. Here we present results on *time-resolved* spectroscopy of *non-perturbative, off-resonance* THz sideband generation from *bulk* GaAs.
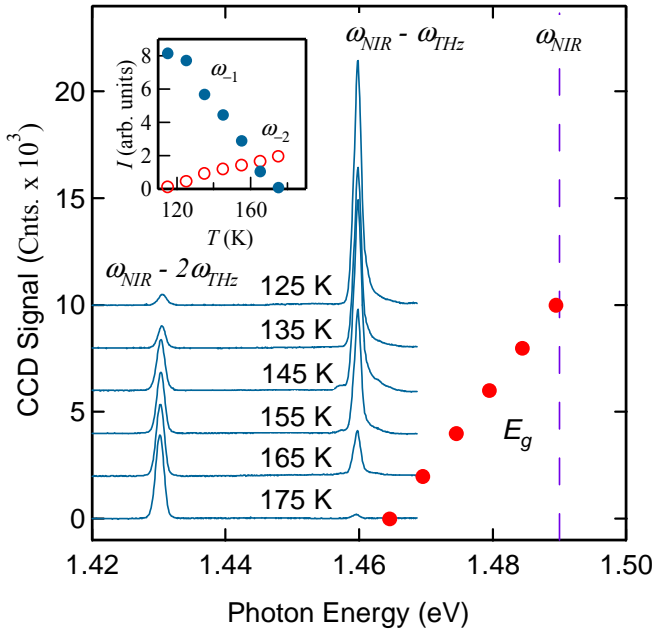
Fig. 9. Sideband spectra at different temperatures. The spectra are offset for clarity. The vertical dashed line denotes the NIR fundamental energy ($\hbar\omega_{NIR}$). The solid circles represent the band gap of the sample as measured by interband absorption spectroscopy for each temperature. Inset: Sideband intensity as a function of temperature. Solid (open) circles represent the experimental values for the ω_{-1} (ω_{-2}) sidebands.

In Fig. 9, we show sideband spectra at selected temperatures, which are vertically offset for clarity. The vertical dashed line represents the energy of the fundamental NIR quantum, $\hbar\omega_{NIR} \approx 1.49$ eV. The solid circles show the band-edge of GaAs for each T, obtained by interband absorption spectroscopy. The intensity of the sidebands is strongly temperature-dependent. As T is raised from 125 K to 175 K, the ω_{-2} sideband increases in intensity whereas the ω_{-1} sideband

decreases and eventually vanishes at $T \approx 180$ K. At higher T (not shown) the ω_{-2} sideband weakens and vanishes at $T \approx 230$ K. This intriguing behavior is related to the interplay between absorption of the NIR fundamental and that of the sidebands; i.e., while a larger density-of-states at the fundamental energy favors more intense sidebands, no real states are desirable at the sideband frequencies, since they will be absorbed. The fact that the ω_{-2} sideband persists to higher T is a direct consequence of its lower energy as compared to the ω_{-1} sideband, in agreement with the temperature dependence of the GaAs bandedge. In the remainder of this section we show data taken only at 160 K, where the sidebands are approximately equal in intensity.
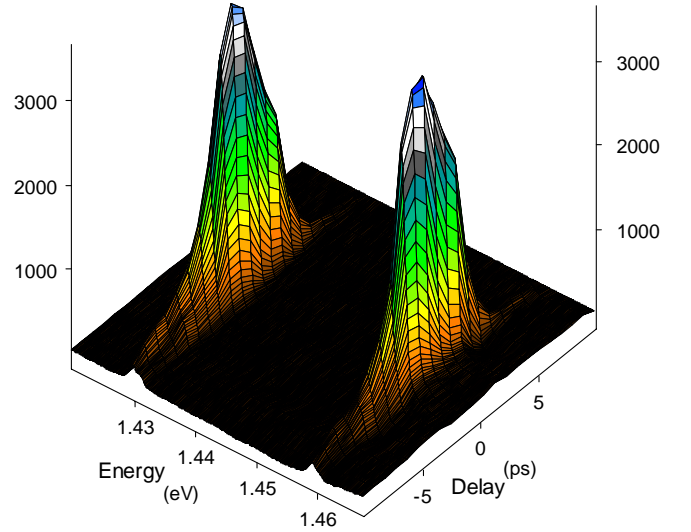
Fig. 10. Sideband intensity as a function of photon energy and relative delay between the NIR and THz pulses. This represents a convenient method for characterizing THz pulses using a Si photodetector.

Since we used picosecond THz pulses, we were able to probe the evolution of the THz sidebands directly in the time domain for the first time. Using the delay stage, we can change the temporal overlap between the NIR and THz pulses (e.g., from -10 ps to +10 ps) and acquire a series of sideband spectra at selected time delay values. The result of this procedure is shown in Fig. 10, where we present the intensities of both the ω_{-1} and ω_{-2} sidebands versus both the photon energy $\hbar\omega$ and the relative delay time. We observe that sidebands indeed appear only when the NIR and THz pulses temporally overlap. Given the fact that sidebands remain in the NIR part of the spectrum, we therefore arrive at a new method of measuring the temporal profile of the THz pulses using a Si photodetector.

Finally, we studied how the sideband intensities depend on the THz and NIR intensities. Figures 11(a) and 11(b) show the sideband intensities at 160 K vs. I_{THz} and I_{NIR}, respectively. At low I_{THz}, the ω_{-1} (ω_{-2}) sideband shows a linear (quadratic) dependence, consistent with a perturbative $\chi^{(2)}$ ($\chi^{(3)}$) process involving one (two) THz photons. However, at higher I_{THz}, we observe a significant deviation from the perturbative behavior, which indicates the entrance into a strong THz field regime. A measure of the field strength at which such a deviation is expected is the ponderomotive potential (U_p), i.e., the time-averaged kinetic energy of an

electron in an AC electric field [see Eq. (11) in Section 6]. At our highest THz intensity ($\sim 1.2 \times 10^8$ W/cm^2), U_p is estimated to be about 180 meV, which is 6 times larger than the THz photon energy (30 meV). Thus it is reasonable to expect non-perturbative behavior to occur. Since only one NIR photon is involved in the generation process of either sideband, at low I_{NIR}, we see the expected linear dependence for both the ω_{-1} and ω_{-2} sidebands but it clearly saturates at higher intensities [see Fig. 11(b)]. Since NIR photons create real carriers above the bandedge ($\hbar\omega_{NIR} \approx E_g$), free-carrier absorption of the THz radiation can result in the saturation of the sideband intensity. In addition, the population of the conduction band reduces the number of states that contribute to the sideband generation that are resonant to the fundamental (phase space filling).
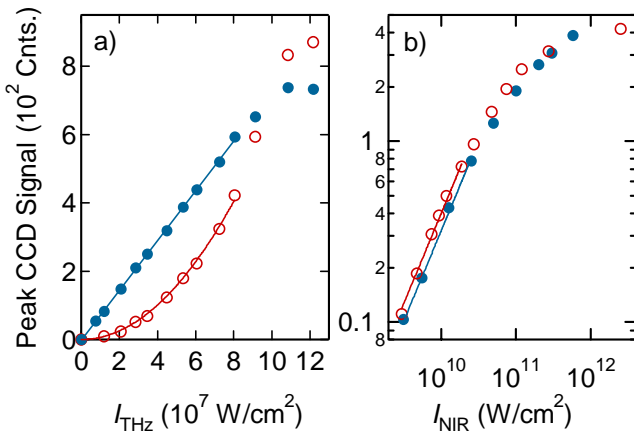

Fig. 11. (a) THz and (b) NIR intensity dependence of the THz intensity. The filled (open) circles represent the ω_{-1} (ω_{-2}) sideband intensity. The solid curves are linear and quadratic fits to the data at low powers.

6. Extreme mid-infrared nonlinear optics

This and the next section describe our experiments using intense MIR radiation from an optical parametric amplifier (OPA).[23,24,34,35] These experiments explore predicted unusual phenomena in strongly laser driven semiconductors. The small photon energies (compared to visible or NIR light) help minimize interband absorption (both linear and multiphoton) and sample damage, while the low dispersion existing at longer wavelengths allows phase-matching over longer distances. Also, for a given laser intensity, the ponderomotive potential (also known as the wiggle or quiver energy) of the driven electron increases quadratically with decreasing photon energy [see Eq. (11) below]. Thus, strong-field physics in solids are more suitably studied using MIR or FIR rather than optical or NIR wavelengths.

The source of intense MIR pulses was an OPA pumped by a Ti:Sapphire based regenerative amplifier. The system produced pulses at a 1 kHz repetition rate with either ~ 1 ps or ~ 200 fs pulse duration, and (with difference-frequency mixing of the signal and idler) wavelengths from 3 μm to 10 μm. For these studies, we used pulses at wavelengths of 3.5 μm or 6.2 μm (where atmospheric absorption is negligible).

To study laser-induced coherent bandgap distortion described in Section 6-1, we measured the transmission near the band edge of bulk semiconductors using broadband light as a probe. The broadband light was produced by continuum generation in a sapphire plate, using the residual pump pulse (800 nm) after the OPA. The broadband probe was temporally overlapped with the MIR pump (or driving field) by changing the time delay (via the optical path length) of the MIR pump relative to the probe. The NIR probe and the MIR pump were focused onto the sample using an off-axis paraboloid, with the beams crossing at $\sim 10°$. After passing through the sample, the spectrum of the broadband probe was dispersed using a grating monochromator and detected using a Si CCD camera (response between 1.1 eV and ~ 3 eV). Spectra were obtained with the driving field at various time delays with respect to the probe, and were subsequently normalized to the probe spectrum without the sample, to obtain the absolute transmission (accurate to $\pm 5\%$).

We studied two types of high-order, multi-photon processes: sideband and harmonic generation, as described in Section 6-2. In sideband generation, we measure the NIR spectrum after nonlinear wave mixing of intense NIR and MIR pulses in a semiconductor. Temporal overlap was achieved by varying the optical path of the MIR beam with respect to the NIR beam. In harmonic generation, we measured the spectrum of intense MIR pulses after transmission through a semiconductor.

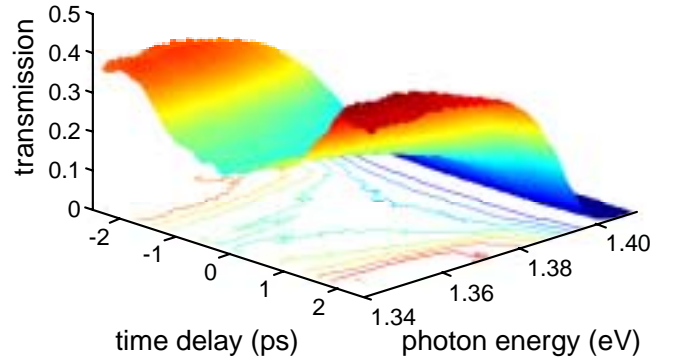### 6-1. Coherent Bandgap Distortion

Fig. 12. Transmission of a NIR broadband probe pulse through GaAs as a function of time delay between the arrival of the intense 3.5 μm MIR driving pulse and the NIR probe pulse.

Shown in Fig. 12 is transmission data taken using a 3.5 μm MIR driving field with ~ 1 ps pulse duration and $\sim 2 \times 10^{10}$ W/cm^2 peak incident intensity. Under these conditions, we observed a dramatic *decrease* in transmission that extends past 0.2 eV below the band edge ($E_g = 1.4$ eV) of the GaAs sample (350 μm thick, semi-insulating, (100) surface). The energy range over which the change occurs is larger than any observed electro-absorption using strong static fields, or energy shift due to intense laser pulses via the AC Stark effect. This decreased transmission, due to induced absorption, occurs only during the presence of the intense MIR pulse. This clearly demonstrates the virtual nature of the effect, i.e., no MIR excitation of carriers across the band gap and/or lattice-

heating effects are involved. The effect is not found to depend on rotation of the sample in the surface plane, suggesting no dependence on crystal orientation, as would be the case with a second-order perturbative $\chi^{(2)}$ process (χ is the optical susceptibility).
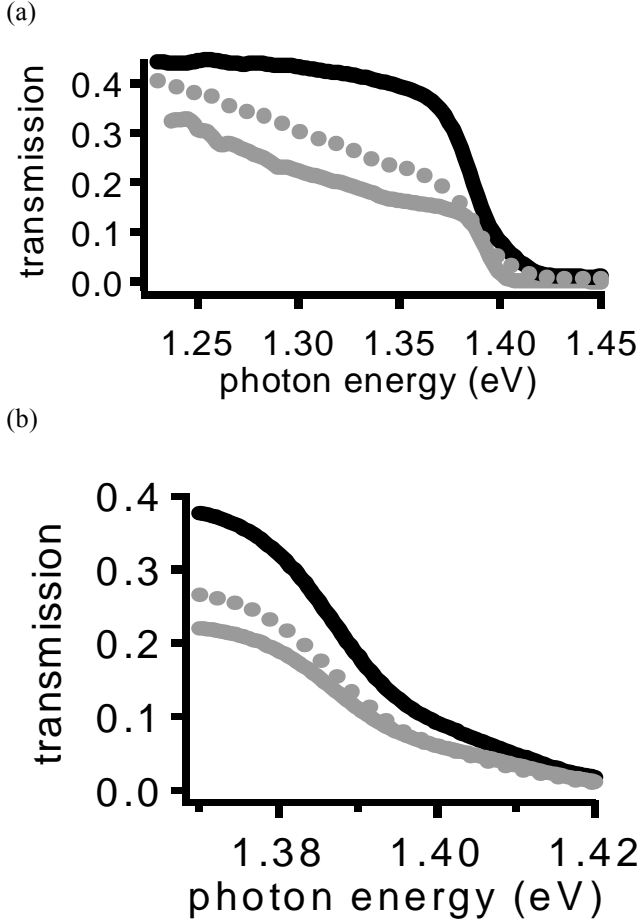
(a)

(b)

Fig. 13. (a) Wavelength dependence of electro-absorption in GaAs: 3.5 μm MIR driving pulse (gray), 6.2 μm MIR driving pulse (gray dashed), and no driving pulse (black). (b) Intensity dependence: I_0 (gray), $I_0/2$ (gray dashed), and with no driving pulse (black).

Shown in Fig. 13(a) is the wavelength dependence of the effect in GaAs, comparing the 3.5 μm and 6.2 μm cases with $\sim 3 \times 10^9$ W/cm^2 peak intensity. Here, we observe an effect in the 6.2 μm case that is comparable to the 3.5 μm case, but the cutoff occurs closer to the band edge, due to the smaller MIR photon energy. Shown in Fig. 13(b) is the intensity dependence of the effect in GaAs using 3.5 μm MIR driving pulses, which is consistent with an absorption coefficient that is linearly dependent on the driving field intensity. Finally, the effect is not specific to GaAs, as we also observed induced absorption in polycrystalline ZnSe (E_g = 2.7 eV) and crystalline ZnTe (E_g = 2.3 eV). The induced absorption in ZnSe (3 mm thick) with and without the presence of a 3.5 μm MIR driving field is shown in Fig. 14. Our measurements clearly demonstrate not only the magnitude of the effect, but also the extent ($\sim$ 1 eV below the band edge) of the

absorption induced by MIR pulses, which far exceeds any previously observed induced absorption in semiconductors.
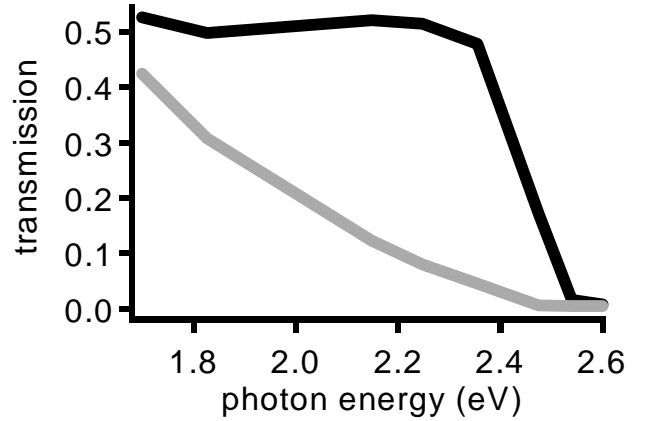

Fig. 14. Transmission below the band edge of ZnSe with (gray) and without (black) an intense 3.5 μm MIR driving field.

A measure of the field strength required to observe nonperturbative phenomena is the ponderomotive potential (also known as the wiggle or quiver energy), i.e., the time-averaged kinetic energy of an electron in an AC electric field. For a driving AC electric field with vector potential $\vec{A} = \vec{A}_0 e^{i\omega t}$, the ponderomotive potential is given by

$$U_p = \frac{e^2 A_0^2}{4mc^2} = \left(\frac{2\pi e^2}{mc} \right)\left(\frac{I}{\omega^2} \right), \quad (11)$$

where I is the intensity of the electric field at frequency ω, and m is the mass of the electron. Existing models predict a laser-induced absorption with an absorption coefficient that is linear with the ponderomotive potential and with an extent that is on the order of the ponderomotive potential (or photon energy, since $U_p \sim \hbar\omega$ in our experiments) below the band edge.[36–42] Both of these predictions are consistent with our data. Using a model based on the Bloch-Volkov wavefunctions, and the theory of x-ray absorption in gases in the presence of a strong laser field, we simulated the data in GaAs driven by a 3.5 μm MIR driving field. There is good agreement between our model and our observations.[23]

6-2. Multiple-photon processes

Typical MIR sideband generation data is shown in Fig. 15. Here, the 800 nm (1.55 eV) NIR probe pulse spectrum is significantly modified in the presence of intense MIR fields to possess multiple sidebands that are spaced by the MIR photon energy. The data in Fig. 15 was obtained in polycrystalline ZnSe (3mm thick) using $\sim$ 1 ps pulses of either 3.5 μm wavelength (0.35 eV) with peak intensity of $\sim 2 \times 10^{10}$ W/cm^2 or 6.2 μm wavelength (0.22 eV) with peak intensity of $\sim 3 \times 10^9$ W/cm^2. We observed sum-frequency and difference-frequency mixing ($\pm$ 1 MIR photon sidebands) as well as higher-order wave mixing, with up to $\pm$ 3 MIR photon sidebands (with 6.2 μm MIR pulses) observed in the spectral range of the detectors used. Previous studies of sideband generation in semiconductors relied on resonant

enhancement of the nonlinear optical susceptibility.[14,32] Here, we observed multiple non-resonant sidebands in semiconductors. The ± 1 (± 2) MIR photon sidebands are linearly (quadratically) dependent on the MIR intensity up to the maximum MIR intensity used in these experiments. All of the sidebands are linearly dependent on the NIR intensity. We also observed multiple optical sidebands in ZnS and ZnTe, demonstrating the lack of system specificity due to the nonresonant nature of wave mixing.
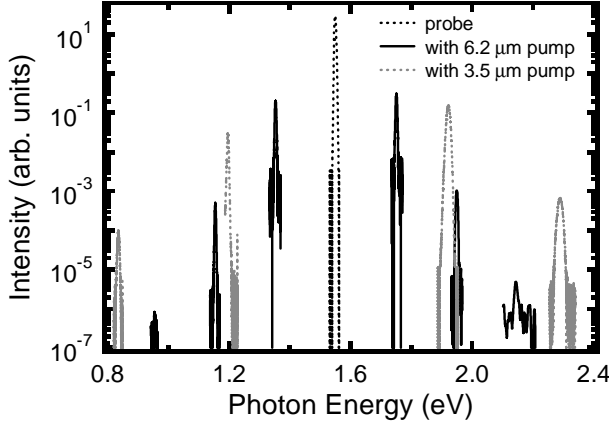

Fig. 15. Optical sidebands in polycrystalline ZnSe generated when a MIR pump pulse and a 800 nm (1.55 eV) probe pulse (dashed line) are overlapped.

Figure 16 shows the sideband spectra as a function of time delay between 3.5 μm MIR and 800 nm NIR pulses for the ~ 1 ps pulses in polycrystalline ZnSe (3 mm thick) for ± 1 MIR sidebands. The sideband spectra change in both intensity and peak location as the NIR pulse interacts with different temporal sections of the MIR pulse.
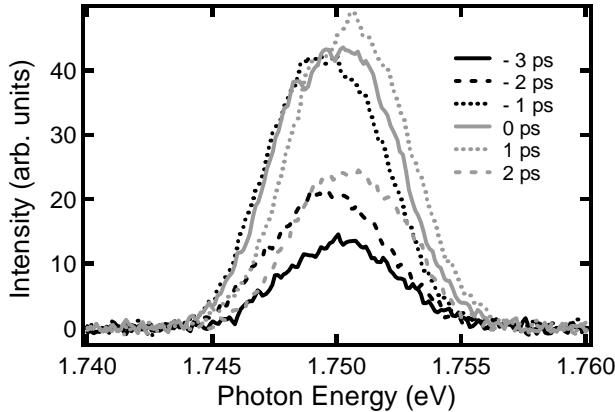

Fig. 16. -1 sideband spectra in polycrystalline ZnSe for different time delays between 6.2 μm (0.22 eV) MIR pulses at ~ 3×10⁹ W/cm² and 800 nm (1.55 eV) NIR pulses.

Figure 17(a) shows the multiple harmonics observed in polycrystalline ZnS (2 mm thick) using ~ 1 ps pulses at 3.5 μm, with a peak intensity of ~ 2×10^{10} W/cm². Up to the maximum MIR intensity using the picosecond pulses, the second, third, and fourth harmonics are measured to have quadratic, cubic, and quartic dependence with the MIR intensity, respectively. While third and higher harmonics have been observed from solid surfaces,[43,44] and MIR harmonics have been observed in gases[45] and liquids,[46] we observed

multiple (up to fifth harmonic) MIR harmonics in *bulk* semiconductors. With higher MIR intensity (~ 10^{11} W/cm²) using shorter (~ 200 fs) pulses at ~ 3.9 μm, we also observed an interesting broadening of the spectrum (in excess of the transform limited bandwidth) of MIR harmonics. An extreme case of this broadening is shown in Fig. 17(b), where multiple (up to seventh) MIR harmonics are seen to exhibit both spectral broadening, and overlap between the harmonics to form what we refer to as a harmonic-continuum.
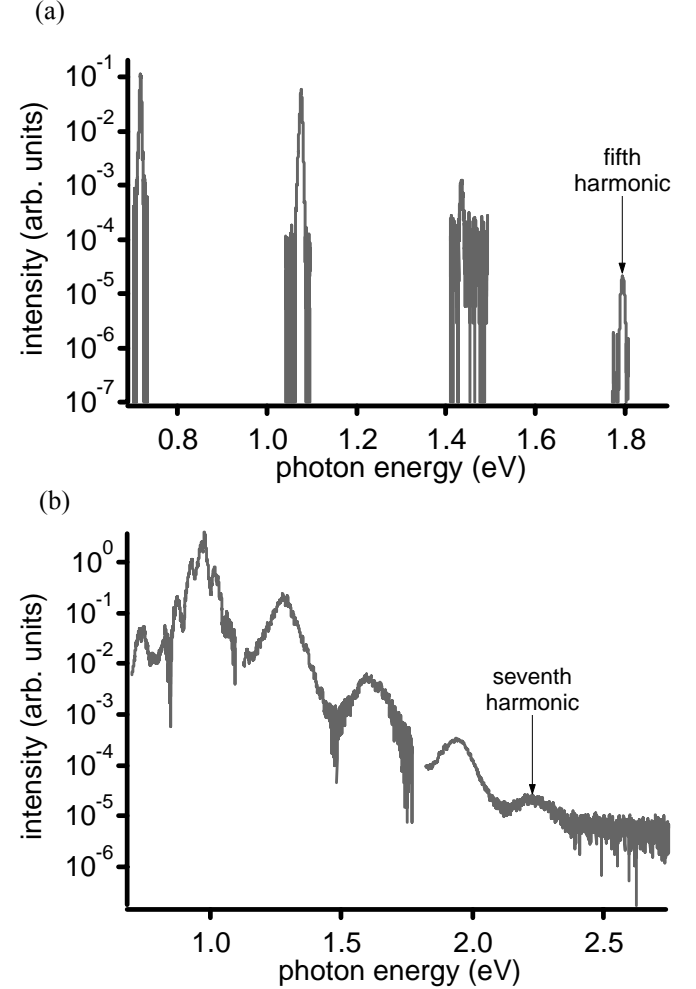

Fig. 17. (a) MIR harmonics in ZnS using 3.5 μm (0.35 eV), ~ 1 ps, ~ 2×10^{10} W/cm² MIR pulses. (b) MIR harmonics in ZnSe using ~ 3.9 μm (0.32 eV), ~ 200 fs, ~ 10^{11} W/cm² MIR pulses.

We believe that several factors contribute to the generation of the observed extreme MIR nonlinear optical phenomena by minimizing phase mismatch between the beams. Two such factors are the low dispersion that exists at wavelengths in between phonon absorption and interband absorption in semiconductors, and the long wavelengths used. Low dispersion allows a longer interaction length for sideband/harmonic generation. To illustrate this point, consider the case of second harmonic generation in GaAs in regions of low and high dispersion. To generate the second harmonic using a fundamental wavelength of 6 μm (low dispersion), the interaction length is ~ 75 μm, whereas to generate second harmonic using a fundamental wavelength of 1.6 μm (high dispersion), the interaction length is ~ 1 μm. Longer

wavelengths intrinsically yield longer interaction lengths due to the slower phase variation. Consequently, the generation of sidebands/harmonics is more efficient at longer wavelengths. In spite of these factors, the estimated interaction lengths (~ 10 μm) are still much shorter than the sample thicknesses used here (~ 1 mm). Thus, without any spectral modifications, significant phase mismatch exists in the samples.

One factor that can alleviate the remaining phase mismatch is the influence of self-phase modulation (SPM) of the fundamental on sideband/harmonic generation, which is known as cross-phase modulation (XPM).[47-49] Under the excitation conditions used, significant phase shifts due to SPM are expected to occur in the MIR beam. For example, using ~ 2 × 10^{10} W/cm^2 at a wavelength of 3.5 μm passing through 350 μm of GaAs, the estimated intensity-induced phase shift is ~ 1 radian. Self-phase modulation generates additional bandwidth in the fundamental, which alleviates any strong thickness dependence of phase matching through XPM by providing a distribution of wavevectors that contributes to each sideband/harmonic wavelength. This consequence of XPM, in combination with the low dispersion and long wavelength light used, allows multiple sideband/harmonic generation to be more easily observable using MIR rather than visible fundamental frequencies. To verify this, we performed numerical calculations that take into account $\chi^{(3)}$ processes involving SPM of the MIR, $\chi^{(N)}$ processes for the sideband/harmonic generation process under the influence of XPM, and the appropriate phase matching.[34] We obtained good agreement between calculations and data.

7. Excitons in intense, high-frequency AC fields

The nonlinear optical response of excitons in quantum wells has been, and continues to be, a subject of intense research, due to the potential applications. One of these potential applications is ultrafast optical modulation via ultrafast electroabsorption in excitons.[50] The response of excitons to strong field transients,[51] strong, low frequency fields (photon energy less than the binding energy),[52] and strong tehahertz fields (photon energy comparable to the binding energy),[13,15,53–55] have been studied previously.

Here we are considering an applied field whose strength is sufficient to cause field-ionization at a frequency where the photon energy of the applied field is larger than the ionization energy. This regime has not previously been examined in atomic or semiconductor systems. At first glance, either field-ionization or photoionization should lead to quenching of the exciton resonance. However, we observe that under such conditions, the exciton resonance remains relatively unaffected. We attribute this resistance to quenching to the mismatch between the period of the applied field, and the response time of the exciton.[51] The experimental setup used to study the exciton response to strong, high frequency fields is the same as the setup described in Section 6.
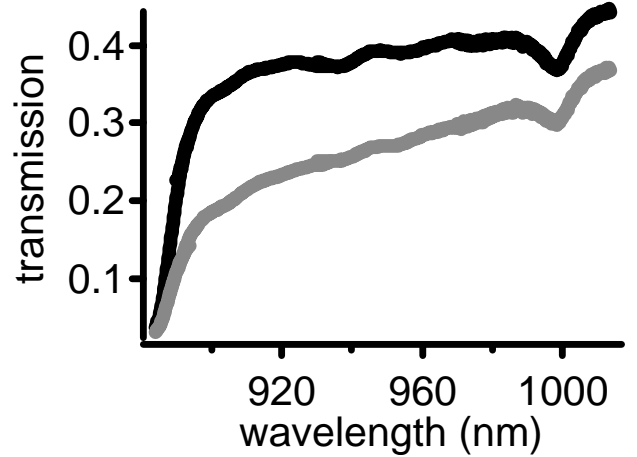

Fig. 18. Transmission below the GaAs band edge of a quantum well sample on a GaAs substrate. The black curve represents data with no applied field. The gray curve represents data with a 3.5 μm driving field with ~ 2 × 10^{10} W/cm^2 peak intensity (~4 × 10^6 V/cm peak field). The reduction in transmission is due to the dynamical Franz-Keldysh effect (see text). Note the continued exciton resonance at 1000 nm, even with the strong, high frequency field.
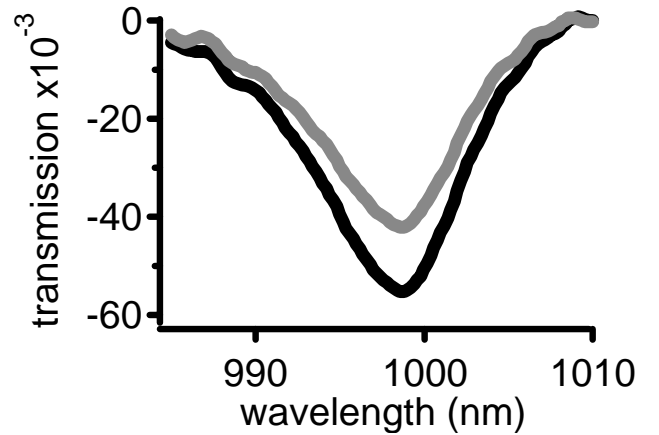

Fig. 19. Transmission around the exciton resonance of the quantum well sample from the data shown in Fig. 18. The black curve represents data with no applied field. The data is modified to subtract the transmission data around the exciton absorption peak in order to subtract the DFKE in the substrate.

Figure 18 shows transmission data taken using ~ 1 ps, 3.5 μm MIR (86 THz) pulses with peak intensity of ~ 2 × 10^{10} W/cm^2 (~4 × 10^6 V/cm peak field) compared to data taken without the strong, high frequency field. The MIR beam is at nearly normal incidence to the sample, so that the MIR electric field is primarily in the plane of the quantum wells and perpendicular to the growth direction. The reduction in transmission near 1000 nm is the 1s exciton resonance associated with the transition between the highest hole subband (H1) and the lowest electron subband (E1) in the quantum wells. The reduction in transmission around 890 nm is the band edge of the GaAs substrate. The primary feature of the data obtained in the presence of the strong MIR field is the overall reduction of transmission over the wavelength range shown. This is due to the dynamical Franz-Keldysh effect in

the GaAs substrate, and is discussed in detail in Section 6-1. The fact that we observe this effect in the substrate indicates that we are also applying a strong field in the MQW sample that is of sufficient strength to ionize excitons, if the field was applied at a lower frequency. The other feature in the data is that the exciton resonance remains relatively unaffected with the strong MIR field. To better examine any effects on the exciton resonance, we removed the absorption change in the substrate by assuming a baseline on either side of the resonance and subtracting the baseline from the data. Figure 19 shows the result of such data processing. There is a small decrease in the peak amplitude of the exciton resonance in the presence of the MIR field, but there is little broadening apparent in the peak width, as is expected from field-ionization.[52]

We attribute this lack of quenching of the exciton resonance by the strong MIR field to the mismatch between the period of the strong field, and the exciton orbit time. The time scales relevant to exciton response are the exciton orbit time ($\sim h/E_{\text{binding}}$), the electron tunneling time [$\sim (mE_{\text{binding}})^{1/2}/(eF)$, where F is the applied electric field], and the exciton lifetime. Among these relevant time scales, the intrinsic exciton lifetime (estimated to be several hundreds of picoseconds from the homogeneous linewidth), and the lifetime determined by the inhomogeneous linewidth (~ 100 ps), are much longer than the period of the applied field, and thus should not play a role here. Under our conditions, $eF \approx 4 \times 10^6$ eV/cm, $m \approx 0.07m_0$, and $E_{\text{binding}} \sim 10^{-2}$ eV, the tunneling time is ~ 0.2 fs. Since the period of the 3.5 μm MIR field (12 fs) is longer than the tunneling time, the peak field is strong enough to cause field ionization of the exciton. However, the applied field has a photon energy that is larger than the exciton binding energy, i.e., the period of the applied field (12 fs) is significantly shorter than the exciton orbit time $h/E_{\text{binding}} \sim 360$ fs). Thus, the exciton cannot respond to the high frequency field, because the field is trying to drive the exciton at a frequency well above the resonance frequency. In the case of atoms, the analogous response (in the x-ray regime) is a very weak interaction of the valence electrons with the applied field, and therefore a refractive index close to unity and a scattering cross-section approaching the free-electron value (i.e., no resonance enhancement). In our case, with 0.35 eV MIR photons and $E_{\text{binding}} \sim 10^{-2}$ eV, we have a relative frequency of $\omega/\omega_{\text{resonance}} \approx 30$, and a damping factor of $\gamma/\omega_{\text{resonance}} \approx 0.5$, which is in a frequency region where no significant resonance enhancement occurs. Therefore, {\em the strong, high frequency field views the exciton as a free electron and hole, not as a bound pair.}

Another ionization mechanism for these strong, high frequency fields that could affect the exciton resonance is photoionization. Since the photon energy (0.35 eV) of the high frequency field is much greater than the exciton binding energy (~ 0.01 eV), photoionization of the exciton is allowed. However, assuming exciton photoionization behaves like atomic photoionization, which scales as $(E_{\text{photon}} - E_{\text{binding}})^{-7/2}$ (where E_{photon} is the photon energy of the applied field), the photoionization probability decreases rapidly with increasing photon energy above the ionization threshold. This is related to the lack of resonant enhancement stated

above, i.e., photoionization is greatest when the incident photon energy is resonant with the relevant binding energy. In our case, we should have a photoionization probability that is $\sim 4 \times 10^{-6}$ times that of the photoionization probability near resonance. Nevertheless, we do observe evidence of a decrease (see Fig. 19) in the excitonic absorption in the presence of the strong, high frequency field, which may be due to this photoionization process.

In conclusion, we have observed that a quantum-confined exciton does not respond strongly to a high frequency field (i.e., well above the exciton resonant frequency) that would cause field-ionization at a lower frequency. We attribute this lack of field-ionization to the fact that the exciton response time is slow relative to the period of the strong field. These observations represent some of the possible strong-field phenomena that may be studied in excitons in semiconductors that are very difficult to observe in atoms, due to the lack of intense ultraviolet sources.

8. Summary

We have explored ultrafast and nonlinear optical phenomena in semiconductor-based systems at long wavelengths (or small photon energies) using intense, coherent, and tunable radiation from a far-infrared free electron laser, and a mid-infrared optical parametric amplifier. A series of recent experiments were described in this article, i.e., far-infrared spectroscopy of transient plasmas and magneto-plasmas, far-infrared picosecond time-resolved cyclotron resonance, far-infrared and mid-infrared sideband and harmonic generation, the dynamical Franz-Keldysh effect, and AC ionization dynamics of quantum-well excitons. Most of these experiments were carried out by using a synchronized, two-color (far-infrared/near-infrared or mid-infrared/near-infrared) system, which allowed us to couple with intra- and interband transitions simultaneously. Some of the nonlinear optical experiments were made possible by taking advantage of small-energy (or long-wavelength) photons, which help minimize interband absorption and sample damage while employing the low dispersion existing at longer wavelengths and maximizing the ponderomotive potential.

9. Acknowledgements

References

1) See, e.g., W. B. Colson, E. D. Johnson, M. J. Kelley, and H. A. Schwettman, Physics Today **55**, 35 (2002).

2) See, e.g., M. K. Reed and M. K. Steiner-Shepard, IEEE J. of Quantum. Electron. **32**, 1273 (1996).

3) See, e.g., M. C. Nuss and J. Orenstein, in *Millimeter and Submillimeter Wave Spectroscopy of Solids*, ed. G. Gruener (Springer, Berlin, 1998), pp. 7-50.

4) D. Some and A. V. Nurmikko, Phys. Rev. B **50**, 5783 (1994).

5) T. A. Vaughan, R. J. Nicholas, C. J. G. M. Langerak, B. N. Murdin, C. R. Pidgeon, N. J. Mason, and P. J. Walker, Phys. Rev. B **53**, 16481 (1996).

6) S. K. Singh, B. D. McCombe, J. Kono, S. J. Allen, I. Lo, W. C. Mitchel, and C. E. Stutz, Phys. Rev. B **58**, 7286 (1998).

7) B. N. Murdin, A. R. Hollingworth, M. Kamal-Saadi, R. T. Kotitschke, C. M. Ciesla, C. R. Pidgeon, P. C. Findlay, H. P. M. Pellemans, C. J. G. M. Langerak, A. C. Rowe, R. A. Stradling, and E. Gornik, Phys. Rev. B **59**, R7817 (1999).

8) J. Kono, A. H. Chin, A. P. Mitchell, T. Takahashi, and H. Akiyama, Appl. Phys. Lett. **75**, 1119 (1999).

9) A. P. Mitchell, A. H. Chin, and J. Kono, Physica B **272**, 434 (1999).

10) P. C. M. Planken, P. C. van Son, J. N. Hovenier, T. O. Klaassen, W. Th. Wenckebach, B. N. Murdin, and G. M. H. Knippels, Phys. Rev. B **51**, 9643 (1995).

11) S. R. Ryu, G. S. Herold, J. Kono, M. S. Salib, B. D. McCombe, J. P. Kaminski, and S. J. Allen, Superlattices and Microstructures **21**, 241 (1997).

12) B. E. Cole, J. B. Williams, B. T. King, M. S. Sherwin, and C. R. Stanley, Nature **410**, 60 (2001).

13) J. Černe, J. Kono, M. S. Sherwin, M. Sundaram, A. C. Gossard, and G. E. W. Bauer, Phys. Rev. Lett. **77**, 1131 (1996).

14) J. Kono, M. Y. Su, T. Inoshita, T. Noda, M. S. Sherwin, S. J. Allen, and H. Sakaki, Phys. Rev. Lett. **79**, 1758 (1997).

15) K. B. Nordstrom, K. Johnsen, S. J. Allen, A.-P. Jauho, B. Birnir, J. Kono, T. Noda, H. Akiyama, and H. Sakaki, Phys. Rev. Lett. **81**, 457 (1998).

16) H. P. M. Pellemans and P. C. M. Planken, Phys. Rev. B **57**, R4222 (1998).

17) N. A. van Dantzig and P. C. M. Planken, Phys. Rev. B **59**, 1586 (1999).

18) R. A. Kaindl, S. Lutgen, M. Woerner, T. Elsaesser, B. Nottelmann, V. M. Axt, T. Kuhn, A. Hase, and H. Kunzel, Phys. Rev. Lett. **80**, 3575 (1998).

19) R. A. Kaindl, M. Wurm, K. Reimann, M. Woerner, T. Elsaesser, C. Miesner, K. Brunner, and G. Abstreiter, Phys. Rev. Lett. **86**, 1122 (2001).

20) J. N. Heyman, R. Kersting, and K. Unterrainer, Appl. Phys. Lett. **72**, 644 (1998).

21) G. B. Serapiglia, E. Paspalakis, C. Sirtori, K. L. Vodopyanov, and C. C. Phillips, Phys. Rev. Lett. **84**, 1019 (2000).

22) M. Y. Su, C. Phillips, J. Ko, L. Coldren, and M. S. Sherwin, Physica B **272**, 438 (1999).

23) A. H. Chin, J. M. Bakker, and J. Kono, Phys. Rev. Lett. **85**, 3293 (2000).

24) A. H. Chin, O. G. Calderon, and J. Kono, Phys. Rev. Lett. **86**, 3292 (2001).

25) N. Dai, F. Brown, P. Barsic, G. A. Khodaparast, R. E. Doezema, M. B. Johnson, S. J. Chung, K. J. Goldammer, and M. B. Santos, Appl. Phys. Lett. **73**, 1101 (1998).

26) See, e.g., B. K. Ridley, *Quantum Processes in Semiconductors, Fourth Edition* (Oxford University Press, Oxford, 1999), p. 175.

27) See, e.g., E. D. Palik and J. K. Furdyna, Rep. Prog. Phys. **33**, 1193 (1970).

28) See, e.g., B. D. McCombe and R. J. Wagner, in: Vol. 37 of *Advances in Electronics and Electron Physics*, ed. L. Marton (Academic Press, New York, 1975), pp. 1-78.

29) K. Johnsen, Phys. Rev. B **62**, 10978 (2000).

30) T. Inoshita, Phys. Rev. B **61**, 15610 (2000).

31) D. S. Citrin, Phys. Rev. B **60**, 13695 (1999).

32) C. Phillips, M. Y. Su, M. S. Sherwin, J. Ko, and L. Coldren, Appl. Phys. Lett. **75**, 2728 (1999).

33) T. Inoshita, J. Kono, and H. Sakaki, Phys. Rev. B **57**, 4604 (1998).

34) O. G. Calderón, A. H. Chin, and J. Kono, Phys. Rev. A **63**, 053807 (2001).

35) A. H. Chin, J. Kono, and G. S. Solomon, Phys. Rev. B **65**, 121307(R) (2002).

36) Y. Yacoby, Phys. Rev. **169**, 610 (1968).

37) Yu. I. Balkarei and E. M. Epshtein, Sov. Phys. Solid State **15**, 641 (1973).

38) H. D. Jones and H. R. Reiss, Phys. Rev B **16**, 2466 (1977).

39) H. R. Reiss, Phys. Rev. A **22**, 1786 (1980).

40) L. C. M. Miranda, Solid State Commun. **45**, 783 (1983).

41) O. A. C. Nunes, J. Appl. Phys. **58**, 2102 (1985).

42) K. Johnsen and A.-P. Jauho, Phys. Rev. B **57**, 8860 (1998).

43) Y.-S. Lee, M. H. Anderson, and M. C. Downer, Opt. Lett. **22**, 973 (1997).

44) T. Tsang, Phys. Rev. A **54**, 5454 (1996).

45) B. Sheehy, J. D. D. Martin, L. F. DiMauro, P. Agostini, K. J. Schafer, M. B. Gaarde, and K. C. Kulander, Phys. Rev. Lett. **83**, 5270 (1999).

46) R. Zürl and H. Graener, Appl. Phys. B **66**, 213 (1998).

47) A. M. Zheltikov, N. I. Koroteev, and A. N. Naumov, JETP **88**, 857 (1999).

48) P. P. Ho, Q. Z. Wang, D. Ji, T. Jimbo, and R. R. Alfano, Appl. Phys. Lett. **54**, 111 (1989).

49) P. C. M. Planken, L. Kuipers, and A. Lagendijk, Phys. Rev. A **42**, 4085 (1990).

50) W. H. Knox, D. A. B. Miller, and T.C. Damen, Appl. Phys. Lett. **48**, 864 (1986).

51) S. Schmitt-Rink, D. S. Chemla, W. H. Knox, and D. A. B. Miller, Opt. Lett. **15**, 60 (1990).

52) D. A. B. Miller, D. S. Chemla, T. C. Damen, A. C. Gossard, W. Wiegmann, T. H. Wood, and C. A. Burrus, Phys. Rev. B **32**, 1043 (1985).

53) S. M. Quinlan, A. Nikroo, M. S. Sherwin, M. Sundaram, and A. C. Gossard, Phys. Rev. B **45**, 9428 (1992).

54) J. Černe, A. G. Markelz, M. S. Sherwin, S. J. Allen, M. Sundaram, A. C. Gossard, P. C. van Son, and D. Bimberg, Phys. Rev. B **51**, 5253 (1995).

55) J. Černe, J. Kono, M. Su, and M. S. Sherwin, cond-mat/0207327.